

1 **Pore constrictions in intervessel pit membranes provide a mechanistic explanation for xylem**
 2 **embolism resistance in angiosperms**

3 Lucian Kaack^{1*}, Matthias Weber^{2*}, Emilie Isasa³, Zohreh Karimi⁴, Shan Li⁵, Luciano Pereira¹,
 4 Christophe L. Trabi¹, Ya Zhang⁶, H. Jochen Schenk⁷, Bernhard Schuldt³, Volker Schmidt², Steven
 5 Jansen¹

6 ¹Institute of Systematic Botany and Ecology, Albert-Einstein-Allee 11, Ulm University, D-89081
 7 Ulm, Germany

8 ²Institute of Stochastics, Helmholtzstraße 18, Ulm University, D-89069 Ulm, Germany

9 ³Ecophysiology and Vegetation Ecology, Julius-von-Sachs-Institute for Biological Sciences,
 10 University of Würzburg, Julius-von-Sachs-Platz 3, D-97082 Würzburg, Germany

11 ⁴Department of Biology, Faculty of Sciences, Golestan University, Shahid Beheshti St, Gorgan
 12 15759-49138, Iran

13 ⁵Department of Wood Anatomy and Utilization, Research Institute of Wood Industry, Chinese
 14 Academy of Forestry, Beijing 100091, China

15 ⁶College of Life Sciences, Anhui Normal University, Beijingdong Road 1, Wuhu 241000, China

16 ⁷Department of Biological Science, California State University Fullerton, Fullerton, CA 92834-
 17 6850, USA

18 Corresponding author: lucian.kaack@uni-ulm.de

19 * Both authors contributed equally to this study.

Total word count (excluding summary, acknowledgements, references and legends)	6756	No. of Figures	7 (Figs 2-7 in colour)
Summary	200	No. of Tables	4
Introduction	1598	No. of Supporting Information	12 (Fig. S1-S6; Table S1; Methods S1-S5)
Material and Methods	1053		
Results	1447		
Discussion	2658		
Acknowledgements	98		

20 SUMMARY

- 21 • Embolism spreading in angiosperm xylem occurs via mesoporous pit membranes between
22 vessels. Here, we investigate how the size of pore constrictions in pit membranes is related
23 to pit membrane thickness and embolism resistance.
- 24 • Pit membranes were modelled as multiple layers to investigate how pit membrane
25 thickness and the number of intervessel pits per vessel determine pore constriction sizes,
26 the probability of encountering large pores, and embolism resistance. These estimations
27 were complemented by measurements of pit membrane thickness, embolism resistance,
28 and number of intervessel pits per vessel in stem xylem ($n = 31, 31, \text{ and } 20$ species,
29 respectively).
- 30 • The modelled constriction sizes in pit membranes decreased with increasing membrane
31 thickness, explaining the measured relationship between pit membrane thickness and
32 embolism resistance. The number of pits per vessel affected constriction size and embolism
33 resistance much less than pit membrane thickness. Moreover, a strong relationship between
34 modelled and measured embolism resistance was observed.
- 35 • Pore constrictions provide a mechanistic explanation why pit membrane thickness
36 determines embolism resistance, and suggest that hydraulic safety can be uncoupled from
37 hydraulic efficiency. Although embolism spreading remains puzzling and encompasses
38 more than pore constriction sizes, angiosperms are unlikely to have leaky pit membranes,
39 which enables tensile transport of water.

40

41 Keywords: angiosperm xylem, embolism, embolism propagation, pit membrane, pore constriction,
42 porous medium, vessel, ultrastructural modelling

43

44 INTRODUCTION

45 Xylem sap in vessel-bearing angiosperms crosses numerous intervessel walls from the root
46 to the leaf xylem, depending on the plant size, vessel length, intervessel connectivity, and vessel
47 network topology (Loepfe *et al.*, 2007). It is well known that small openings in the secondary cell
48 wall, which are described as bordered pits, play an important role in hydraulic transport between

49 adjacent vessels, and also in failure of the transport system by gas entry, i.e. embolism (Choat *et*
50 *al.*, 2008; Kaack *et al.*, 2019). Since water transport efficiency is tightly related to transpiration
51 and photosynthesis, drought-induced embolism formation can have major implications for plant
52 performance, especially under drought (Li *et al.*, 2016; Sorek *et al.*, 2021). Yet, many details about
53 the mechanistic relationship between embolism formation and the anatomical determinants of pits
54 remain to be clarified.

55 An angiosperm vessel is estimated to have a median of about 14,188 intervessel pits, with
56 values for different species varying more than 200-fold, from ca. 500 pits to > 100,000 (sample
57 size, $n = 72$ species; Fig. S1 based on data from literature). Each bordered pit pair has a pit
58 membrane, which is mainly composed of ca. 20 nm wide cellulose microfibril aggregates. These
59 pit membranes develop from the primary cell wall and middle lamella, and have a mean diameter
60 of $4.8 \pm 2.4 \mu\text{m}$ ($n = 43$ species; Jansen *et al.*, 2009, 2011). Before pit membranes become
61 hydraulically functional, hemicellulose and pectin compounds are enzymatically removed
62 (O'Brien, 1970; Herbette *et al.*, 2015; Klepsch *et al.*, 2016). Therefore, fully mature pit membranes
63 are non-woven, fibrous porous media of mainly cellulose, with a thickness between ca. 160 and
64 1,000 nm (Esau 1977; Pesacreta *et al.*, 2005; Kaack *et al.*, 2019).

65 Pit membranes control the immediate entry of gas from neighbouring, embolised conduits,
66 and may become sites of further embolism propagation under persistent drought (Zimmermann,
67 1983; Brodersen *et al.*, 2013; Choat *et al.*, 2016; Brodribb *et al.*, 2016; Roth-Nebelsick, 2019).
68 Embolism spreading from an embolised vessel to a sap-filled vessel has been described as “air-
69 seeding”, but the actual mechanism underlying embolism formation represents one of the major
70 knowledge gaps in our understanding of water transport in plants (Jansen *et al.*, 2018). It is
71 assumed that propagation of drought-induced embolism from one vessel to a neighbouring vessel
72 is affected among other factors by pore dimensions of intervessel pit membranes. Here, we use the
73 broader term embolism spreading or propagation instead of air-seeding because embolism
74 spreading includes both mass flow and diffusion of gas across pit membranes. Air-seeding,
75 however, is limited to mass flow only, and embolism formation may not be caused only by mass
76 flow of gas (Guan *et al.*, In press). Also, embolism is used instead of the term cavitation, because
77 the triggering process leading to embolism is unlikely due to the formation of a void by phase
78 transition from liquid to gas, but most likely caused by pre-existing bubbles (Hölttä *et al.*, 2002;
79 Schenk *et al.*, 2017).

80 Instead of perfectly flat, two-dimensional structures, pit membranes are porous media with
81 pores that include multiple constrictions, with the respective narrowest constriction in each pore
82 governing flow of water and gas (Fig. 1; Kaack *et al.*, 2019) and, consequently, embolism
83 spreading. Estimates of bottleneck diameters, *i.e.* constriction sizes, vary from 5 nm to well above
84 200 nm (Choat *et al.*, 2003; Sano, 2005; Jansen *et al.*, 2009; Hillabrand *et al.*, 2016). Part of this
85 variation is caused by sample preparation for imaging by scanning electron microscopy (SEM),
86 which induces up to 50% shrinkage of T_{PM} during drying, with frequently enlarged pores and
87 cracks (Shane *et al.*, 2000; Jansen *et al.*, 2008; Zhang *et al.*, 2017). Moreover, the challenge is to
88 quantify the size and shape of pit membrane pores in a three-dimensional approach. A three-
89 dimensional model based on transmission electron microscopy (TEM) of fresh and shrunken pit
90 membranes indicated a high porosity (*i.e.* void volume fraction) of 81%, highly interconnected
91 pores with non-tortuous, unbending passageways, a lack of dead-end pores, and the occurrence of
92 multiple pore constrictions within a single pore (Zhang *et al.*, 2020). Based on a shrinkage model
93 and gold perfusion experiments, it has been found that constriction sizes in pit membrane pores
94 vary from 5 to < 50 nm, with an average diameter around 20 nm (Choat *et al.*, 2003, 2004; Zhang
95 *et al.*, 2020). The evidence available suggests that pore sizes are fairly constant for angiosperm
96 species, despite considerable variation in T_{PM} . Indeed, pore constriction sizes around 20 nm occur
97 both in species with thin (ca. 200 nm) and thick (> 500 nm) pit membranes (Fig. S2), and there is
98 no evidence for large (> 50 nm) pore size differences among species (Zhang *et al.*, 2020). However,
99 Zhang *et al.* (2020) recorded only which gold particle sizes were able to penetrate pit membranes,
100 and did not quantitatively report the penetration depth and frequency distribution of gold particles.
101 Could small differences in pore constriction sizes and frequencies in pit membranes explain the
102 relatively variable xylem embolism resistances within angiosperms (Choat *et al.*, 2012)?

103 Angiosperm species with thick pit membranes were found to be more resistant to drought-
104 induced embolism than species with thin pit membranes (Jansen *et al.*, 2009; Li *et al.*, 2016; Dória
105 *et al.*, 2019; Trueba *et al.*, 2019; Levionnois *et al.*, 2020; Thonglim *et al.*, 2020). This functional
106 link between T_{PM} and P_{50} , which is the xylem water potential corresponding to 50% loss of the
107 maximum hydraulic conductivity (P_{50} , MPa), is valid at the interspecific (Li *et al.*, 2016),
108 intrageneric level (Lens *et al.*, 2011; Plavcová & Hacke, 2012; Scholz *et al.*, 2013) and
109 intraspecific level (Schuldt *et al.*, 2016). Variation in T_{PM} is mainly determined by the number of
110 microfibril layers (N_L), with thin pit membranes consisting of fewer microfibril layers than thick

111 pit membranes. Note that N_L can be estimated by assuming that cellulose fibres have a diameter of
112 about 20 nm (Pesacreta *et al.*, 2005), and 20 nm pore spaces between each layer based on gold
113 perfusion experiments (Table 1; Zhang *et al.*, 2020). As such, pit membranes with a thickness
114 between 140 and 1,180 nm (Jansen *et al.*, 2009; Li *et al.*, 2016) include between 4 and 30 layers.
115 In our models, bottlenecks in a given pore are formed by the pore constrictions between cellulose
116 fibres within a single layer. Therefore, the number of constrictions within a pore (N_C) equals N_L
117 (Table 1). Since it is unknown why thin pit membranes are more vulnerable to embolism than thick
118 pit membranes (Jansen *et al.*, 2018), we explore the hypothesis that the likelihood of leaky pores
119 with wide pore constrictions is affected by N_L , which could explain why T_{PM} is related to P_{50} .

120 The mismatch between pore size estimations based on colloidal gold perfusion and
121 experimental values of embolism resistance resulted in the hypothesis that a very small percentage
122 of pit membranes might contain large pores (Choat *et al.*, 2003, 2004). These rare pit membrane
123 pores are assumed to cause low embolism resistance. The idea of such leaky, rare pits was further
124 enhanced when variation in P_{50} at an interspecific level was found to decrease with increasing pit
125 membrane surface area in intervessel walls (Wheeler *et al.*, 2005). The “pit area hypothesis”
126 (Sperry *et al.*, 2006), which was later termed “rare pit hypothesis”, provided a possible explanation
127 for high vulnerability to embolism, and relied on a largely two-dimensional interpretation of pit
128 membranes (Hacke *et al.*, 2007; Christman *et al.*, 2009, 2012; Plavcová *et al.*, 2013). While the
129 rare pit hypothesis follows a plausible mechanism that seems well supported by indirect evidence,
130 it cannot be tested because the existence of a rare pit with a large pore cannot be observed directly,
131 and is impossible to be verified from a statistical point of view. However, a three-dimensional
132 modelling approach to estimate the likelihood of leaky pits is clearly lacking.

133 The number of layers in a pit membrane may affect the size of the narrowest constriction
134 within a pore that crosses the entire intervessel pit membrane. If embolism propagation is at least
135 to some extent determined by the radius of a pore, the most important dimension of a pore is its
136 minimum diameter, i.e., the diameter of the narrowest bottleneck along the pore (R_{MIN} , nm). We
137 can think of this diameter as the “effective diameter” of the pore. The entry of an air-water
138 meniscus or a bubble in a pit membrane is determined by the pore with the largest effective
139 diameter within the pit membrane. Thus, embolism spreading and the minimum hydraulic
140 resistance at the intervessel level are governed by the pore with the largest effective diameter in
141 all pit membranes of a single vessel.

142 First, we hypothesise that the effective diameter of each pore becomes smaller with
143 increasing T_{PM} and N_L , as proposed in Kaack *et al.* (2019) (Hypothesis 1). This hypothesis is
144 investigated at the individual pit membrane level based on a stochastic pit membrane model.
145 Second, we hypothesise that model-based values of embolism spreading largely agree with
146 embolism resistance measurements for a large number of species (Hypothesis 2). Third, we expect
147 that the probability of having a leaky pit membrane is low at the whole vessel level, and affected
148 by both T_{PM} (Li *et al.*, 2016), and the total number of intervessel pits per vessel (N_{PIT} ; Hypothesis
149 3) (Wheeler *et al.*, 2005). The second hypothesis is tested based on experimental data on embolism
150 resistance, and anatomical measurements, while two further stochastic pit membrane models are
151 developed to test the third hypothesis. Testing these hypotheses should help us to better understand
152 the functional link between embolism resistance and pit membrane ultrastructure.

153

154 MATERIALS AND METHODS

155 Pit membrane modelling

156 To better understand the relationship between T_{PM} and embolism resistance, we developed
157 three complementary pit membrane models. For reasons of simplicity, we assumed the existence
158 of more or less cylindrical pores, which govern transport phenomena, and modelled each pore as
159 a three-dimensional object instead of a circular, flat opening (Sperry and Hacke, 2004; Mrad *et al.*,
160 2018). Following the multi-layered pit membrane model of Zhang *et al.* (2020), we assumed that
161 each pore penetrates a fixed number of microfibril layers (N_L). Each of these layers induces a pore
162 constriction of some random radius (Fig. 1e). An important property of each pore is its effective
163 radius, i.e., the radius of the narrowest pore constriction within the entire pore (R_{MIN} , nm). We
164 were especially interested in how R_{MIN} was affected by T_{PM} (Hypothesis 1), how modelled
165 embolism resistance based on pore constriction size related to measured embolism resistance
166 (Hypothesis 2), and to what extent the likelihood of leaky pit membranes at the entire vessel level
167 was affected by T_{PM} and/or N_{PIT} (Hypothesis 3).

168 We developed a first model to estimate pit membrane leakiness at the structural level of a
169 single pit membrane, and two models estimating leakiness at the vessel level. Detailed model
170 descriptions and implementations are provided in the Supplementary Information (Methods S1,
171 S2, S3).

172 **Model 1. Pore constrictions in single intervessel pit membranes**

173 In this model (Fig. 2a), we assumed circular pit membranes with a diameter of 5 μm
 174 (estimated from $n = 43$ species, based on Jansen *et al.* 2009, 2011), each comprising a fixed number
 175 of pores (N_P), which were defined by a fixed number of pore constrictions (N_C). The random radius
 176 of each pore constriction was modelled by applying left-truncated normal distributions around
 177 mean constriction sizes of 20 nm (Scenario 1) and 100 nm (Scenario 2) in diameter to obtain an
 178 upper bound for the number of pores that fit into the membrane, resulting in N_P -values of 12,000
 179 and 1,100, respectively.

180 For T_{PM} -values between 140-1340 nm, we simulated random diameters of pore
 181 constrictions of a whole pit membrane and estimated the probability of encountering at least one
 182 pore larger than 35 nm (Scenario 1) or 180 nm (Scenario 2) in a pit membrane, as well as the mean
 183 and maximum constriction sizes (R_{MIN_mean} , R_{MIN_max}) of the effective radii R_{MIN} . R_{MIN_mean} and
 184 R_{MIN_max} were compared to the experimental data on embolism resistance with calculated
 185 embolism propagation pressures based on a modified Young-Laplace equation.

186 **Models 2. Leaky pit membranes without hole alignment at the vessel level**

187 Model 2 investigated the occurrence of leaky pit membranes at the vessel level (Fig. 2b)
 188 for T_{PM} values between 50-1200 nm and N_{PIT} values up to 400,000. Upper bounds for the
 189 probability of encountering at least one large pore, spanning an entire intervessel pit membrane
 190 with an effective radius larger than t were calculated based on the probabilities P of encountering
 191 a large hole in any given layer P^{NL} for $P = 0.25$ (Scenario 1) and $P = 0.50$ (Scenario 2). A large
 192 pore through the pit membrane was assumed to exist if there was at least one large hole in each
 193 layer. At the entire vessel level, an upper bound for the probability of encountering a leaky pit
 194 membrane (P_{LP}) was given by

195
$$P_{LP} = 1 - (1 - P^{NL})^{N_{PIT}} \text{ [Eqn 2].}$$

196 Values of N_{PIT} ranging from 510 to 370,755, with a median of 14,188, were calculated by dividing
 197 the total pit membrane surface area per vessel (A_P) by the corresponding pit areas (A_{PIT}) of 72
 198 species using original data and literature data (Fig. S1; Wheeler *et al.*, 2005; Jansen *et al.*, 2011;
 199 Lens *et al.*, 2011; Nardini *et al.*, 2012; Scholz *et al.*, 2013; Klepsch *et al.*, 2016).

200 **Model 3. Leaky pit membranes with hole alignment at the vessel level**

201 Model 3 considered the alignment of holes within successive layers by modelling pit
 202 membranes as stacks of circular cellulose layers (according to N_L). The pit membranes had a
 203 diameter D_P of 5 μm , and each layer was perforated by a fixed number of holes (N_{HOLES}) of 5
 204 (Scenario 1) or 10 (Scenario 2). The holes were randomly located in each layer and had radii $t \geq$
 205 100 nm. The locations of holes within and across layers were simulated stepwise and repeated 10^6
 206 times for pit membranes with N_L -values between 3 and 23 (corresponding to T_{PM} -values of 100-
 207 900 nm; Table 1). A pore did only traverse all layers if there existed a sequence of holes that were
 208 aligned for each pair of adjacent layers (Fig. 2c). For each scenario, we estimated the probability
 209 that at least one hole with $t \geq 100$ nm crossed an entire pit membrane and the probability of
 210 encountering one large pore in a vessel with 30,000 intervessel pits (N_{PIT}). Minimum overlap of
 211 holes between adjacent layers was assumed to be sufficient for embolism spreading, even if only
 212 their edges were overlapping.

213 **Experimental work**

214 The three models were complemented by experimental data on embolism resistance ($n = 31$
 215 species), T_{PM} measurements at the centre ($T_{\text{PM_centre}}$) and near the edges ($T_{\text{PM_edge}}$) ($n = 31$ species),
 216 and the total intervessel pit membrane area per average vessel (A_P , $n = 20$ species). The methods
 217 applied to obtain these data included well-established, previously published protocols (Wheeler *et*
 218 *al.*, 2005; Sperry *et al.*, 2006; Schuldt *et al.* 2016; Zhang *et al.* 2020; Kotowska *et al.*, 2020), and
 219 are described in detail in the Supporting Information (Methods S4). All data included original
 220 measurements, except for data retrieved from literature for embolism resistance of five species,
 221 and for A_P values of four species.

222 **Statistics and data processing**

223 Data processing, simulations and statistical analyses were performed using Excel, R, and Matlab.
 224 Shapiro-Wilk Tests were applied to test for normal distribution. Pearson's Correlation Coefficient
 225 were used to test for linear correlation. Basic linear and non-linear regressions were fitted to test
 226 whether P_{12} , P_{50} , P_{88} , and the slope of vulnerability curves (S) were related to T_{PM} or A_P , and could
 227 be estimated. For each of the 31 species studied, we estimated embolism resistance by integrating
 228 their modelled $R_{\text{MIN_mean}}$ and $R_{\text{MIN_max}}$, based on T_{PM} , into the equations of the relation between
 229 T_{PM} and embolism propagation pressure of Model 1 (Equations 3 and 4, Methods S5). This

230 approach allowed us to compare estimated embolism propagation with experimental values of P_{12}
 231 and P_{50} .

232

233 RESULTS

234 How likely are large pores in a pit membrane for a wide range of T_{PM} ?

235 Average values of R_{MIN} (R_{MIN_mean}) are very low in Scenario 1 of Model 1, with values
 236 below 4.5 nm for pit membranes with 150 to 1,150 nm in thicknesses (Fig. 3a). The size of R_{MIN}
 237 declines considerably with increasing T_{PM} , and the largest values (R_{MIN_max}) decrease from radii of
 238 ca. 20.4 ± 1.4 nm (standard deviation, σ_R) to 6 ± 0.6 nm (Fig. 3a). R_{MIN_max} -values are at least 2.4
 239 times and up to 4.9 times larger than the R_{MIN_mean} -values, decreasing with T_{PM} (Fig. 3a). The
 240 likelihood of having an effective diameter ≥ 35 nm approaches zero (0.00005 ± 0.00009 , Fig. 3b)
 241 when T_{PM} is > 220 nm, or $N_L \geq 6$, thus only occurs in 0.2 out of 12,000 pores.

242 For Scenario 2 of Model 1, a similar decline of R_{MIN} with increasing T_{PM} is found (Fig. S3),
 243 but with steeper declining likelihood values for large pores with T_{PM} . For a T_{PM} of 220 nm the
 244 likelihood of containing a large pore (defined in Scenario 2 of Model 1 as ≥ 180 nm in diameter)
 245 is nearly zero.

246 How does T_{PM} relate to measured embolism resistance?

247 The values of T_{PM_mean} vary from 165 nm ($\pm 18 \sigma_R$) for *Tilia platyphyllos* to 610 nm (± 79
 248 σ_R) for *Olea europaea*, and the median of T_{PM} is equal to 270 nm ($n = 31$ species studied; Table
 249 S1). The value of T_{PM_centre} is always larger than the value of T_{PM_edge} , with an average difference
 250 of 105 nm, varying from 2.1 nm (*Tilia platyphyllos*) to 297 nm (*Olea europaea*), and this difference
 251 increases with T_{PM} . While there is no relation between T_{PM_centre} values and the coefficient of
 252 variation of T_{PM_centre} values (Pearson's Correlation Coefficient, $r(29) = 0.09$, $p > 0.05$), the range
 253 between minimum and maximum values of T_{PM} measured within a tissue strongly increase with
 254 increasing T_{PM} (Pearson's Correlation Coefficient, $r(29) = 0.79$, $p < 0.001$). Thus, species with the
 255 thinnest and thickest pit membranes (*T. platyphyllos* and *O. europaea*) show a T_{PM} range of 80 nm
 256 and 497 nm, respectively.

257 When considering the whole dataset of 31 species studied, P_{50} -values are strongly related
 258 to the values of T_{PM_centre} (Table 3; Fig. 4a), with a logarithmic regression showing an R^2 -value of

259 0.57 ($F(2, 29) = 32.0, p < 0.001$). An outlier in the T_{PM} vs. P_{50} relationship includes *Corylus*
 260 *avellana*, which shows considerably high T_{PM} -values of ca. 400 nm for a P_{50} -value of -2.02 MPa.
 261 Slightly lower correlations are found between the T_{PM_centre} and P_{12} ($F(2, 29) = 24.4, R^2 = 0.46, p$
 262 < 0.001), and between T_{PM_centre} and P_{88} ($F(2, 29) = 34.2, R^2 = 0.54, p < 0.001$; Table 3; Fig. 4a).
 263 The T_{PM_centre} -values show a stronger relationship to embolism resistance than T_{PM_mean} and
 264 T_{PM_edge} . The average intervessel pit membrane surface area per vessel (A_P , Table S1) shows much
 265 lower correlations to P_{12} , P_{50} , and P_{88} than all T_{PM} traits, with the strongest correlation between A_P
 266 and P_{12} ($F(2, 18) = 7.75, R^2 = 0.30, p < 0.05$; Table 3).

267 When limiting our dataset to species with an average intervessel pit membrane surface area
 268 per vessel (A_P) only, no linear correlation between P_{12} , P_{50} , or P_{88} and A_P can be found (Fig. 4c),
 269 whereas correlations of T_{PM_mean} , T_{PM_centre} , and T_{PM_edge} with P_{12} , P_{50} , and P_{88} are negative and
 270 highly significant (Table 4, Fig. 4b).

271 Furthermore, we find a power regression with an R^2 -value of 0.48 between the slope of
 272 vulnerability curves (S) and T_{PM_mean} ($F(2, 29) = 88.4, R^2 = 0.48, p < 0.001$; Table 3), with
 273 decreasing S being associated with increasing T_{PM_mean} . There is a weaker relation between S and
 274 T_{PM_edge} , and a slightly stronger relation with T_{PM_centre} than T_{PM_mean} (Table 3). Thus, thicker pit
 275 membranes result in more negative P_{50} values and a lower slope, with T_{PM} affecting P_{12} and P_{88}
 276 less than P_{50} values.

277 **Does modelled and measured embolism resistance correspond to each other for a wide** 278 **range of T_{PM} ?**

279 There are clear differences in the estimated pressures that would induce embolism
 280 spreading, depending on the surface tension, and whether the maximum or mean R_{MIN} values are
 281 considered (Fig. 4a). For a surface tension of 72 mN/m, estimated pressures of embolism
 282 spreading, which may largely correspond to P_{12} , are much higher than the P_{12} values measured,
 283 and even higher than P_{50} measurements (Fig. S4). Regression lines of the T_{PM} - P_{12} , T_{PM} - P_{50} and
 284 T_{PM} - P_{88} relationship, however, fall well within the estimated embolism propagation pressures
 285 when a surface tension of 25 mN/m (Fig. 4a) is considered. Although absolute values of modelled
 286 and measured embolism resistance (P_{12} and P_{50}) do not match (Fig. 4a, 5), they are significantly
 287 related to each other (Pearson's Correlation Coefficient, P_{12} to R_{MIN_mean} and R_{MIN_max} : $r(29) = 0.67$
 288 and $r(29) = 0.64, p < 0.01$; P_{50} to R_{MIN_mean} and R_{MIN_max} : $r(29) = 0.74$ and $r(29) = 0.73, p < 0.001$;

289 Table 3, Fig. 5). When $R_{\text{MIN_max}}$ is considered, estimated pressures related to embolism spreading
 290 show a small range, with about 1.2 MPa for a T_{PM} of 140 nm and up to 2.7 MPa for a T_{PM} of 758
 291 nm (Fig. 5b), which underestimates embolism resistance (Fig. 4a, 5a, 5b). Much higher embolism
 292 propagation pressures between 5.6 and 10 MPa are obtained for estimations based on $R_{\text{MIN_mean}}$,
 293 thus overestimating embolism resistance (Fig. 5c, d). There is a clear upper limit of embolism
 294 propagation pressure for $R_{\text{MIN_mean}}$ around ca. 10 MPa, which is achieved for pit membranes with
 295 thicknesses ≥ 600 nm (Fig. 4a).

296 Modelled embolism propagation pressures based on $R_{\text{MIN_max}}$ are similar but typically
 297 lower than the experimental values (Fig. 5a, b). Estimated embolism propagation pressures based
 298 on $R_{\text{MIN_max}}$ are especially close to measured embolism resistance for various species with not very
 299 negative P_{12} and P_{50} values (Fig. 5a, b), while estimated embolism propagation pressures based on
 300 $R_{\text{MIN_mean}}$ are much higher than P_{12} and P_{50} measurements (Fig. 5c, d).

301 **How likely are leaky intervessel pit membranes at the vessel level?**

302 Based on Model 2, the probability of having a leaky pit membrane in a vessel decreases
 303 exponentially with increasing T_{PM} (Fig. 6, Fig. S5). For a fixed T_{PM} , the slope of the relationship
 304 between N_{PIT} and the probability of a leaky pore strongly depends on T_{PM} (Fig. S6): steep,
 305 exponential slopes are found for thin pit membranes, while low, more linear slopes are found for
 306 thick pit membranes. Therefore, $T_{\text{PM_mean}}$ and N_{PIT} affect the likelihood of large effective pore radii
 307 differently, with N_{PIT} having an unequal effect on the likelihood of having leaky pit membranes.

308 For the 0.5 likelihood assumption (Fig. S5, S6b), vessels with 820 nm thick pit membranes
 309 reach a likelihood of having a leaky pit membrane below 0.20, even in vessels with 400,000
 310 intervessel pits, which means that not even every fifth vessel would have a leaky pit.

311 For the 0.25 likelihood of Model 2 (Fig. 6, S6a), an exponential change is found for
 312 $T_{\text{PM_mean}}$ -values between 200 and 300 nm, while little or no effect is seen for $T_{\text{PM_mean}}$ -values below
 313 200 nm and above 350 nm. The high and low probability plateaus in the three-dimensional graphs
 314 of Model 2 (Fig. 6, S5) suggest the existence of a thin and a thick T_{PM} -range that typically results
 315 in leaky or very safe, non-leaky vessels, respectively, independent of N_{PIT} . At the exponential
 316 phase of the three-dimensional graph in Fig. 6, an increase in N_{PIT} from 3,000 to 70,000 (i.e. a 23-
 317 fold increase) is equivalent to adding about five additional microfibril layers to a pit membrane

318 (i.e. an increase in T_{PM} of 180 nm). Critical T_{PM} -values are higher for the 0.5 likelihood of Model
 319 2 (Fig. S6b, S5), with the largest effect of N_{PIT} for pit membranes between 500 and 700 nm.

320 The results obtained from Model 3 show that the modelled probability of encountering
 321 leaky pit membranes in a vessel with 30,000 intervessel pits (N_{PIT}) decreases exponentially for
 322 T_{PM} -values above 180 nm or 260 nm when assuming 5 or 10 holes per microfibril layer (N_{HOLES}),
 323 respectively (Fig. 7). Assuming N_{HOLES} of 5 or 10, less than one out of 30,000 pits has a large pore
 324 for T_{PM} -values above 220 nm and 340 nm, respectively. Therefore, 220 nm thick pit membranes
 325 with a N_{HOLES} -value of 5 have a similar safety as 340 nm thick pit membranes with an N_{HOLES} -
 326 value of 10. When directly comparing Model 2 and 3 using 30,000 as value for N_{PIT} , a more or less
 327 similar probability of encountering a large pore in a vessel is found for the 0.25 likelihood scenario
 328 of Model 2 and the 10 holes per layer in Model 3 (Fig. 7).

329

330 DISCUSSION

331 The results described above indicate that the chance of having large pores in pit membranes
 332 decreases strongly with the number of constrictions, and therefore T_{PM} (Hypothesis 1). This finding
 333 is independent of the actual size of pore constrictions, and supported by a strong relation between
 334 embolism resistance and T_{PM} (Jansen *et al.*, 2009, 2018; Lens *et al.*, 2011; Scholz *et al.*, 2013;
 335 Schuldt *et al.*, 2016; Li *et al.*, 2016). Modelled embolism propagation values are significantly
 336 related to measured embolism resistance (Hypothesis 2), although they differ in absolute values.
 337 There is a good agreement when the dynamic surface tension of xylem sap is taken into account
 338 (Yang *et al.*, 2020), but embolism spreading does not seem to represent a function of pore
 339 constriction size (R_{MIN_max} and R_{MIN_mean}) only. Our results also suggest that the likelihood of
 340 having a leaky pit membrane within a vessel is extremely low (Hypothesis 3), and mainly
 341 determined by T_{PM} . Overall, pore constrictions provide a mechanistic explanation why embolism
 342 resistance is correlated with T_{PM} , and why pit membranes provide hydraulic safety to angiosperm
 343 xylem.

344 **The most narrow pore constriction becomes strongly reduced in size with increasing T_{PM}**

345 The three models developed show a negative correlation between the simulated pore sizes
 346 and T_{PM} , which is reflected in a low probability of large pores, both at the level of an individual

347 pit membrane and an entire vessel. Based on Model 1, the chance of having a large pore in a pit
348 membrane thicker than 180 nm is close to zero. Interestingly, the thinnest pit membranes measured
349 in this study (ca. 165 to 180 nm) are likely to represent a lower limit for T_{PM} , since earlier records
350 of T_{PM} below 150 nm (Jansen *et al.*, 2009; Li *et al.*, 2016) are likely artefacts due to shrinkage
351 (Zhang *et al.*, 2017, 2018, 2020; Kotowska *et al.*, 2020). Thus, angiosperm pit membranes seem
352 to have at least four or five layers of cellulose microfibrils and pore constrictions, which keeps the
353 number of large pores very low for most species. There is a clear conceptual relationship between
354 the thickness of a fibrous porous medium, and the size of the narrowest pore constriction as also
355 seen for non-woven, fibrous geotextiles that differ in thickness (Aydilek *et al.*, 2007).

356 Model 2 suggests that the probability of encountering large pores in intervessel pit
357 membranes of an average vessel follows an exponential pattern over a fairly narrow range of T_{PM} ,
358 with critical T_{PM} -values between 200 to 300 nm and 500 to 700 nm for a 0.25 and 0.50 likelihood,
359 respectively, of having at least one hole larger than t within a single microfibril layer. Although
360 this likelihood cannot be accurately determined due to our limited understanding of embolism
361 spreading and the ultrastructure of pit membranes, we believe that a realistic likelihood would
362 probably lay around 0.25, with 0.50 being too conservative. This assumption is supported by the
363 steeper increase in embolism resistance within the lower T_{PM} range between 140 to 340 nm than
364 in the higher T_{PM} range, and by the probabilities of large pores in pit membranes approaching zero
365 for $T_{PM} > 250$ nm in Model 1 and 3. We applied a logarithmic regression between P_{12} , P_{50} , P_{88} and
366 T_{PM} (Fig. 4a), unlike a linear scaling that was previously suggested (Lens *et al.*, 2011; Li *et al.*,
367 2016). Interestingly, this logarithmic regression has P_{50} values approaching 10 MPa for a T_{PM} of
368 $> 1,350$ nm, which corresponds to the upper physical limit of both xylem water potential and the
369 maximum T_{PM} -value of angiosperms measured (Vilagrosa *et al.*, 2003; Jansen *et al.*, 2009; Kanduč
370 *et al.*, 2020).

371 A clear limitation of Models 1 and 2 is that the alignment of pore constrictions or holes
372 across all layers of a pit membrane is not considered. Although we do not know whether alignment
373 across different layers is required for mass flow of air across a pit membrane, misalignment could
374 enormously reduce the probability of having a leaky pit membrane and increase tortuosity, because
375 the assumed 20 nm distance between the layers in all three models is low compared to the hole
376 size in Models 2 and 3. Thus, applying stricter criteria to Model 3, such as larger overlap of holes
377 across all layers to obtain a geodesic tortuosity that would be close to 1 (Zhang *et al.*, 2020), would

378 lead to considerably lower probabilities of leaky pit membranes in a vessel. Nevertheless, even the
 379 low amount of overlap applied demonstrates that the chance of having a leaky vessel with 30,000
 380 intervessel pit membranes drastically decreases when T_{PM} -values are around 250 nm (Fig. 7; 0.25
 381 likelihood scenario of Model 2, Model 3). Since the 0.5 likelihood scenario of Model 2 shows a
 382 decrease in leakiness at much higher T_{PM} -values than the other models, we consider the predictive
 383 value and applicability of this scenario as rather low. It is possible that variation in T_{PM} within a
 384 vessel or within the vessel network provides additional chances of leakiness, and small differences
 385 in T_{PM} across organs (Kotowska *et al.*, 2020) could influence embolism resistance. Capturing this
 386 variation, however, is difficult because measuring T_{PM} may not be straightforward, for instance
 387 due to TEM preparation artefacts, aggregation of cellulose fibrils into larger aggregates, and
 388 seasonal shrinkage of pit membranes (Schmid & Machado, 1968; Sorek *et al.*, 2020).

389 The difference between central and marginal T_{PM} questions the modelling assumption of equally
 390 spaced cellulose fibres. The slightly negatively charged cellulose fibres may repel each other and
 391 are more loosely arranged in the centre (Zhang *et al.*, 2016) than near the edges, where the fibres
 392 are firmly anchored into the pectin-rich annulus and primary wall. Although the orientation of
 393 microfibrils may not be completely random and appears to be directed by a dual guidance
 394 mechanism (Chan & Coen, 2020), it seems unlikely that more cellulose fibrils are deposited in the
 395 centre than near the annulus, opposite to torus-bearing angiosperms (Dute, 2015).

396 **How is the size of pore constrictions linked to embolism resistance?**

397 Embolism propagation across pit membranes is strongly dependent on T_{PM} and N_L , which
 398 control the size of the narrowest pore constriction within a pore. Pit membranes are not different
 399 from other non-woven, fibrous porous media, where the pressure required to force a gas bubble
 400 through the medium, the so-called bubble point, is a function of the thickness of the medium and
 401 its overall structure (Aydilek *et al.*, 2007). Comparison of modelled embolism propagation
 402 pressures with measurements of P_{12} , P_{50} and P_{88} show strong correlations, but clear differences in
 403 absolute values for most species (Fig. 5), with P_{12} , P_{50} and P_{88} values falling between the modelled
 404 embolism propagation based on R_{MIN_mean} and R_{MIN_max} (Fig. 4a, 5b, d). As could be expected, P_{12}
 405 values were closest to estimated values based on R_{MIN_max} . In general, this correlation illustrates
 406 that our assumptions in Model 1 are fairly well related to real embolism propagation pressures in
 407 plants. Despite the simplicity of the three-dimensional models in this study and the modified

408 Young-Laplace equation (see below), it is remarkable that our modelled R_{MIN} values of embolism
 409 resistance largely agree with experimental values, without accounting for variables such as
 410 dynamic surface tension of xylem lipids, bubble snap-off, changes in temperature, gas solubility,
 411 and other xylem anatomical traits. Experimental data on the pressure that is needed to induce
 412 embolism in angiosperm xylem shows values between 0.4 and 2 MPa (Choat *et al.*, 2004; Jansen
 413 *et al.*, 2009; Christman *et al.*, 2012; Wason *et al.*, 2018), which is more or less in line with P_{12}
 414 values of a wide range of angiosperm species (Bartlett *et al.*, 2016). Moreover, 65% of the species
 415 in our study show P_{12} values that are more negative than -2 MPa, with an average P_{12} value of -
 416 2.57 MPa, which matches the average P_{12} value of -2.65 MPa of 12 temperate angiosperm species
 417 (Schuldt *et al.*, 2020).

418 Embolism propagation across thin pit membranes seems to be determined by pores similar
 419 in size to $R_{\text{MIN_max}}$ due to the large similarity between measurements of P_{12} and P_{50} with modelled
 420 embolism resistance based on $R_{\text{MIN_max}}$. In contrast, embolism spreading in species with thick pit
 421 membranes is affected by pore sizes that can be close to both $R_{\text{MIN_max}}$ and $R_{\text{MIN_mean}}$ (Fig. 3b, 4a).
 422 This finding is in line with the fact that high values of $T_{\text{PM_mean}}$ show a higher standard deviation
 423 than low $T_{\text{PM_mean}}$ -values, while the slope of vulnerability curves becomes lower for species with
 424 thicker pit membranes. In addition, the standard error values of P_{12} , P_{50} , and P_{88} tend to increase
 425 with increasing embolism resistance (Table S1), i.e. higher variation in embolism resistance and
 426 lower slopes of embolism resistant species could be linked with increasing variation in T_{PM} for
 427 species with thick pit membranes. In fact, $R_{\text{MIN_mean}}$ is expected to provide an upper limit for
 428 embolism resistance, since it is unlikely that pore constrictions smaller than average values (i.e. <
 429 $R_{\text{MIN_mean}}$) will determine embolism spreading. Accordingly, $R_{\text{MIN_max}}$ offers the least resistance to
 430 mass flow of gas moving through a pore space, and provides a good explanation for a lower limit
 431 to embolism spreading.

432 There can be various reasons why modelled embolism resistance does not match the
 433 absolute values of measured P_{12} values. There are three explanations that may not be mutually
 434 exclusive, but could be complementary to each other: First, the values obtained from Model 1 are
 435 based on embolism propagation estimations of a single pit membrane model with a certain
 436 thickness, while P_{12} and P_{50} values represent hydraulically-weighted losses of conductivity at the
 437 vessel network level, which is affected by various structural xylem parameters, such as vessel
 438 grouping and the ratio of T_{PM} and pit membrane area (Levionnois *et al.*, 2020). Second, estimations

439 based on the Young-Laplace equation should be interpreted with caution due to various poorly
 440 known parameters and processes. Embolism formation in a multiphase environment under
 441 negative pressure is highly complicated, for instance, by dynamic surface tension, line tension, the
 442 contact angle of the gas-liquid interface within the pit membrane, and highly variable pore sizes
 443 (Choat *et al.*, 2004; Law *et al.*, 2017; Schenk *et al.*, 2017; Satarifard *et al.*, 2018; Zhang *et al.*,
 444 2020; Li *et al.*, 2020; Yang *et al.*, 2020). Moreover, pore constrictions and porosity could change
 445 if pit membranes become deflected and aspirated against the pit border, which could cause pit
 446 membrane shrinkage, reduced porosity and constrictivity, or rearrangement of microfibrils (Tixier
 447 *et al.*, 2014; Kotowska *et al.*, 2020; Zhang *et al.*, 2017, 2020). Yet, the mechanical properties of
 448 pit membranes remain largely unknown (Tixier *et al.*, 2014).

449 Third, it is also possible that drought-induced embolism spreading does not happen via
 450 mass flow of air-water menisci across intervessel pit membranes, as suggested by the air-seeding
 451 hypothesis. The discovery of surfactant-coated nanobubbles in xylem sap provides a
 452 complementary mechanism of mass flow of gas, and highlights the importance of amphiphilic,
 453 insoluble lipids associated with pit membranes, and bubble snap-off by pore constrictions (Schenk
 454 *et al.*, 2015, 2017, 2018, 2020; Kaack *et al.*, 2019; Park *et al.*, 2019). Moreover, diffusion of gas
 455 molecules between an embolised and an adjacent vessel could represent an additional way of gas
 456 entry triggering embolism formation (Guan *et al.*, In press), which might be largely dependent on
 457 R_{MIN_mean} and less on R_{MIN_max} .

458 **T_{PM} and the number of intervessel pits have different consequences on embolism resistance**

459 We show that T_{PM} is a much stronger determinant of the likelihood of leaky pit membranes
 460 than N_{PIT} and the total intervessel pit membrane surface area (A_P ; Table 4, Fig. 4c). Therefore, our
 461 results do not support the rare pit hypothesis (Wheeler *et al.*, 2005; Sperry *et al.*, 2006) and provide
 462 a novel view on the relationship between N_{PIT} or A_P and embolism resistance. Most importantly,
 463 our Model 2 shows that T_{PM} and N_{PIT} affect the likelihood of encountering wide pores differently,
 464 with contrasting differences for species with a wide range of T_{PM} . The effect of N_{PIT} on vessel
 465 leakiness is limited to a narrow range of critical T_{PM} values, depending on the assumptions made
 466 in Model 2 (Fig. 6, Fig. S5). The idea that large A_P values lead to a high probability of large pore
 467 constrictions in a vessel, can be applied to a certain range of T_{PM} values. However, the hypothesis

468 that large A_P values increase the probability of large pores in each single vessel is highly doubtful
469 based on the available evidence.

470 In a general, simplified way, three functional types of intervessel pit membranes can be
471 distinguished based on T_{PM} (Model 2): (1) a thin, risky type, with relatively large pore
472 constrictions, rather low embolism resistance, and little or no reduced embolism resistance for low
473 values of N_{PIT} , (2) a thick and very safe pit membrane type, with narrow pore constrictions, high
474 embolism resistance, and hardly any reduction of embolism resistance for high N_{PIT} , and (3) an
475 intermediate pit membrane type, with embolism resistance strongly affected by N_{PIT} , where N_{PIT}
476 or other xylem structural traits could potentially be modified during growth to vary embolism
477 resistance in response to the amount of drought experienced. Unfortunately, exact T_{PM} values to
478 define these pit membranes types are unclear. Based on leakiness probabilities that are close to
479 zero for $T_{PM} > 250$ nm based on Model 1 and Scenario 1 of Model 3 (Figure 3 and 7), and due to
480 the decreasing slopes of the measured P_{50} values with increasing T_{PM} , we roughly estimate that
481 T_{PM} values of the intermediate type are between 150 and 300 nm, which is where the high
482 probability drops from 1 to almost 0 in Fig. 6. This would correspond to 60% of the species in our
483 data set. Interestingly, embolism resistance of the risky and safe pit membranes (types 1 and 2) is
484 not or weakly affected by the number of intervessel pits. Since the number of intervessel pits is
485 associated with hydraulic connectivity, which on its turn affects hydraulic conductivity and thus
486 efficiency (Loepfe *et al.*, 2007; Mrad *et al.*, 2018), this finding suggests that hydraulic safety can
487 be uncoupled from hydraulic efficiency. Thus, for a given T_{PM} and considerable variation in N_{PIT} ,
488 hydraulic conductivity could be affected much more by N_{PIT} than hydraulic safety (Fig. 6, S6).
489 Hence, Model 2 provides a novel view on the weak relationship between specific hydraulic
490 conductivity and P_{50} -values of many angiosperm species (Hacke *et al.*, 2006; Loepfe *et al.*, 2007;
491 Gleason *et al.*, 2016, Sanchez-Martinez *et al.*, 2020). It would also be interesting to examine if
492 considerable variation in T_{PM} and N_{PIT} leads to considerable variation in the hydraulic resistance
493 of pit membranes.

494 The rare pit hypothesis relies on the assumption that for successful embolism propagation,
495 there is always at least one large pore per successive intervessel wall within the xylem network.
496 Our results indicate that the rare pit hypothesis cannot explain embolism propagation at the whole
497 vessel network since the functional importance of multiple pore constrictions makes it highly
498 unlikely that many vessels contain a large pore for a wide range of T_{PM} . In fact, earlier studies that

499 tested the rare pit hypothesis should be considered carefully due to possible artefacts in embolism
500 resistance measurements (Wheeler *et al.*, 2013; Torres-Ruiz *et al.*, 2017). Also, no large pores
501 have ever been found in hydrated pit membranes (Schmid & Machado, 1968; Choat *et al.*, 2003,
502 2004; Pesacreta *et al.*, 2005; Jansen *et al.*, 2018; Zhang *et al.*, 2020). Finally, primary cell wall
503 development, including the assembly and deposition of cellulose fibrillar aggregates, involve
504 highly redundant processes by the cytoplasm and its cytoskeleton, reducing the likelihood of large
505 gaps in primary cell walls (Chaffey *et al.*, 1997; Oda & Fukuda, 2013; Bourdon *et al.*, 2017;
506 Sugiyama *et al.*, 2017, 2019).

507 Further progress in understanding embolism spreading in angiosperm xylem will strongly
508 depend on the development of realistic three-dimensional pit membrane and vessel network
509 models (Gaiselmann *et al.*, 2014; Mrad *et al.*, 2018; Li *et al.*, 2019), combined with careful
510 simulations of the chemical and physical interactions within a multiphase environment of gas,
511 water, cellulose, and surfactants.

512

513 **Acknowledgements**

514 Financial support is acknowledged to SJ by a research grant from the Deutsche Forschungsgemeinschaft
515 (DFG, German Research Foundation, project nr. 383393940), to SJ and VS by the Baden-Württemberg
516 Ministerium für Wissenschaft, Forschung und Kunst (project 7533-7-11.10-16), and to HJS and SJ by the
517 National Science Foundation (IOS-1754850). We thank Klaus Körber from the Bavarian State Institute for
518 Viticulture and Horticulture, Veitshochheim, Germany, for granting us access to the Stutel-Arboretum
519 facility, as well as Andreas Lösch and all others involved in the ‘Klimabäume Stutel’ project. We thank
520 various colleagues and three reviewers for fruitful discussions and valuable suggestions.

521

522 **Author contributions**

523 LK, MW, LP, HJS, VS, SJ planned and designed the research. IE, ZK, SL, CT, YZ, BS provided
524 experimental data. LK and MW wrote the manuscript, with input from all co-authors. LK and MW
525 contributed equally.

526

527

528 **References**

- 529 **Aydilek AH, D'Hondt D, Holtz RD. 2007.** Comparative evaluation of geotextile pore sizes
530 using bubble point test and image analysis. *Geotechnical Testing Journal* **30**: 173–181.
- 531 **Bartlett MK, Klein T, Jansen S, Choat B, Sack L. 2016.** The correlations and sequence of
532 plant stomatal, hydraulic, and wilting responses to drought. *Proceedings of the National*
533 *Academy of Sciences* **113**: 13098–13103.
- 534 **Bourdon M, Kalmbach L, Helariutta Y. 2017.** Plant vasculature: selective membrane-to-
535 microtubule tethering patterns the xylem cell wall. *Current biology: CB* **27**: R842–R844.
- 536 **Brodersen CR, McElrone AJ, Choat B, Lee EF, Shackel KA, Matthews MA. 2013.** In vivo
537 visualizations of drought-induced embolism spread in *Vitis vinifera*. *Plant Physiology* **161**:
538 1820–1829.
- 539 **Brodribb TJ, Bienaimé D, Marmottant P. 2016.** Revealing catastrophic failure of leaf
540 networks under stress. *Proceedings of the National Academy of Sciences* **113**: 4865–4869.
- 541 **Chaffey NJ, Barnett JR, Barlow PW. 1997.** Cortical microtubule involvement in bordered pit
542 formation in secondary xylem vessel elements of *Aesculus hippocastanum* L.
543 (Hippocastanaceae): A correlative study using electron microscopy and indirect
544 immunofluorescence microscopy. *Protoplasma* **197**: 64–75.
- 545 **Chan J, Coen E. 2020.** Interaction between autonomous and microtubule guidance systems
546 controls cellulose synthase trajectories. *Current Biology* **30**: 941-947.e2.
- 547 **Choat B, Badel E, Burlett R, Delzon S, Cochard H, Jansen S. 2016.** Noninvasive
548 measurement of vulnerability to drought-induced embolism by x-ray microtomography. *Plant*
549 *Physiology* **170**: 273–282.
- 550 **Choat B, Ball M, Luly J, Holtum J. 2003.** Pit membrane porosity and water stress-induced
551 cavitation in four co-existing dry rainforest tree species. *Plant Physiology* **131**: 41–48.
- 552 **Choat B, Cobb AR, Jansen S. 2008.** Structure and function of bordered pits: new discoveries
553 and impacts on whole-plant hydraulic function. *New Phytologist* **177**: 608–626.
- 554 **Choat B, Jansen S, Brodribb TJ, Cochard H, Delzon S, Bhaskar R, Bucci SJ, Feild TS,**
555 **Gleason SM, Hacke UG, et al. 2012.** Global convergence in the vulnerability of forests to
556 drought. *Nature* **491**: 752–755.
- 557 **Choat B, Jansen S, Zwieniecki MA, Smets E, Holbrook NM. 2004.** Changes in pit membrane
558 porosity due to deflection and stretching: the role of vestured pits. *Journal of Experimental*
559 *Botany* **55**: 1569–1575.
- 560 **Christman MA, Sperry JS, Adler FR. 2009.** Testing the ‘rare pit’ hypothesis for xylem
561 cavitation resistance in three species of *Acer*. *New Phytologist* **182**: 664–674.

- 562 **Christman MA, Sperry JS, Smith DD. 2012.** Rare pits, large vessels and extreme vulnerability
563 to cavitation in a ring-porous tree species. *New Phytologist* **193**: 713–720.
- 564 **Dória LC, Meijs C, Podadera DS, Del Arco M, Smets E, Delzon S, Lens F. 2019.** Embolism
565 resistance in stems of herbaceous Brassicaceae and Asteraceae is linked to differences in
566 woodiness and precipitation. *Annals of Botany* **124**: 1–14.
- 567 **Dute RR. 2015.** Development, structure, and function of torus–margo pits in conifers, ginkgo
568 and dicots. In: Hacke U, ed. *Functional and Ecological Xylem Anatomy*. Cham: Springer
569 International Publishing, 77–102.
- 570 **Esau K. 1977.** *Anatomy of seed plants* (2nd ed). Wiley, New York.
- 571 **Espino S, Schenk HJ. 2009.** Hydraulically integrated or modular? Comparing whole-plant-level
572 hydraulic systems between two desert shrub species with different growth forms. *New*
573 *Phytologist* **183**: 142–152.
- 574 **Gaiselmann G, Tötze C, Manke I, Lehnert W, Schmidt V. 2014.** 3D microstructure
575 modeling of compressed fiber-based materials. *Journal of Power Sources* **257**: 52–64.
- 576 **Gleason SM, Westoby M, Jansen S, Choat B, Hacke UG, Pratt RB, Bhaskar R, Brodribb**
577 **TJ, Bucci SJ, Cao K-F, et al. 2016.** Weak tradeoff between xylem safety and xylem-specific
578 hydraulic efficiency across the world's woody plant species. *New Phytologist* **209**: 123–136.
- 579 **Guan X, Pereira L, McAdam S, Cao KF, Jansen S. In press.** No gas source, no problem: pre-
580 existing embolism may affect non-pressure driven embolism spreading in angiosperm xylem by
581 gas diffusion. *Plant, Cell and Environment*.
- 582 **Hacke UG, Sperry JS, Feild TS, Sano Y, Sikkema EH, Pittermann J. 2007.** Water transport
583 in vesselless angiosperms: conducting efficiency and cavitation safety. *International Journal of*
584 *Plant Sciences* **168**: 1113–1126.
- 585 **Hacke UG, Sperry JS, Wheeler JK, Castro L. 2006.** Scaling of angiosperm xylem structure
586 with safety and efficiency. *Tree Physiology* **26**: 689–701.
- 587 **Herbette S, Bouchet B, Brunel N, Bonnin E, Cochard H, Guillon F. 2015.** Immunolabelling
588 of intervessel pits for polysaccharides and lignin helps in understanding their hydraulic
589 properties in *Populus tremula* × *alba*. *Annals of Botany* **115**: 187–199.
- 590 **Hillabrand RM, Hacke UG, Lieffers VJ. 2016.** Drought-induced xylem pit membrane damage
591 in aspen and balsam poplar. *Plant, Cell & Environment* **39**: 2210–2220.
- 592 **Hölttä T, Vesala T, Perämäki M, Nikinmaa E. 2002.** Relationships between Embolism, Stem
593 Water Tension, and Diameter Changes. *Journal of Theoretical Biology* **215**: 23–38.
- 594 **Jansen S, Choat B, Pletsers A. 2009.** Morphological variation of intervessel pit membranes and
595 implications to xylem function in angiosperms. *American Journal of Botany* **96**: 409–419.

- 596 **Jansen S, Gortan E, Lens F, Gullo MAL, Salleo S, Scholz A, Stein A, Trifilò P, Nardini A.**
597 **2011.** Do quantitative vessel and pit characters account for ion-mediated changes in the hydraulic
598 conductance of angiosperm xylem? *New Phytologist* **189**: 218–228.
- 599 **Jansen S, Klepsch M, Li S, Kotowska M, Schiele S, Zhang Y, Schenk H.** **2018.** Challenges in
600 understanding air-seeding in angiosperm xylem. *Acta Horticulturae* **1222**: 13–20.
- 601 **Jansen S, Pletsers A, Sano Y.** **2008.** The effect of preparation techniques on SEM-imaging of
602 pit membranes. *IAWA Journal* **29**: 161–178.
- 603 **Kaack L, Altaner CM, Carmesin C, Diaz A, Holler M, Kranz C, Neusser G, Odstrcil M,**
604 **Schenk HJ, Schmidt V, et al.** **2019.** Function and three-dimensional structure of intervessel pit
605 membranes in angiosperms: a review. *International Association of Wood Anatomists Journal* **40**:
606 673–702.
- 607 **Kanduč M, Schneck E, Loche P, Jansen S, Schenk HJ, Netz RR.** **2020.** Cavitation in lipid
608 bilayers poses strict negative pressure stability limit in biological liquids. *Proceedings of the*
609 *National Academy of Sciences of the United States of America* **117**: 10733–10739.
- 610 **Karimi Z,** **2014.** Systematic, Evolutionary and Functional Anatomy of Wood and Leaves in
611 Betulaceae. PhD thesis, Ulm University, BW, Germany.
- 612 **Klepsch MM, Schmitt M, Paul JK, Jansen S.** **2016.** The chemical identity of intervessel pit
613 membranes in *Acer* challenges hydrogel control of xylem hydraulic conductivity. *Annals of*
614 *Botany* **PLANTS** **8**.
- 615 **Kotowska MM, Thom R, Zhang Y, Schenk HJ, Jansen S.** **2020.** Within-tree variability and
616 sample storage effects of bordered pit membranes in xylem of *Acer pseudoplatanus*. *Trees* **34**:
617 61–71.
- 618 **Law BM, McBride SP, Wang JY, Wi HS, Paneru G, Betelu S, Ushijima B, Takata Y,**
619 **Flanders B, Bresme F, et al.** **2017.** Line tension and its influence on droplets and particles at
620 surfaces. *Progress in Surface Science* **92**: 1–39.
- 621 **Lens F, Sperry JS, Christman MA, Choat B, Rabaey D, Jansen S.** **2011.** Testing hypotheses
622 that link wood anatomy to cavitation resistance and hydraulic conductivity in the genus *Acer*.
623 *The New Phytologist* **190**: 709–723.
- 624 **Levionnois S, Jansen S, Wandji RT, Beauchêne J, Ziegler C, Coste S, Stahl C, Delzon S,**
625 **Authier L, Heuret P.** (2020) Linking drought-induced xylem embolism resistance to wood
626 anatomical traits in Neotropical trees. *New Phytologist* doi.org/10.1111/nph.16942.
- 627 **Li S, Feifel M, Karimi Z, Schuldt B, Choat B, Jansen S.** **2016.** Leaf gas exchange
628 performance and the lethal water potential of five European species during drought. *Tree*
629 *Physiology* **36**: 179–192

- 630 **Li S, Lens F, Espino S, Karimi Z, Klepsch M, Schenk HJ, Schmitt M, Schuldt B, Jansen S.**
631 **2016.** Intervessel pit membrane thickness as a key determinants of embolism resistance in
632 angiosperm xylem. *IAWA Journal* **37**: 152–171.
- 633 **Li S, Wang J, Yin Y, Li X, Deng L, Jiang X, Chen Z, Li Y.** **2020.** Investigating effects of
634 bordered pit membrane morphology and properties on plant xylem hydraulic functions — A case
635 study from 3D reconstruction and microflow modelling of pit membranes in angiosperm xylem.
636 *Plants* **9**: 231.
- 637 **Loepfe L, Martinez-Vilalta J, Piñol J, Mencuccini M.** **2007.** The relevance of xylem network
638 structure for plant hydraulic efficiency and safety. *Journal of Theoretical Biology* **247**: 788–803.
- 639 **Mrad A, Domec J-C, Huang C-W, Lens F, Katul G.** **2018.** A network model links wood
640 anatomy to xylem tissue hydraulic behaviour and vulnerability to cavitation. *Plant, Cell &*
641 *Environment* **41**: 2718–2730.
- 642 **Nardini A, Dimasi F, Klepsch M, Jansen S.** **2012.** Ion-mediated enhancement of xylem
643 hydraulic conductivity in four *Acer* species: relationships with ecological and anatomical
644 features. *Tree Physiology* **32**: 1434–1441.
- 645 **O’Brien TP.** **1970.** Further observations on hydrolysis of the cell wall in the xylem.
646 *Protoplasma* **69**: 1–14.
- 647 **Oda Y, Fukuda H.** **2013.** Rho of plant GTPase signaling regulates the behavior of Arabidopsis
648 Kinesin-13A to establish secondary cell wall patterns. *The Plant Cell* **25**: 4439–4450.
- 649 **Park J, Go T, Ryu J, Lee SJ.** **2019.** Air spreading through wetted cellulose membranes:
650 Implications for the safety function of hydraulic valves in plants. *Physical Review E* **100**:
651 032409.
- 652 **Pesacreta TC, Groom LH, Rials TG.** **2005.** Atomic force microscopy of the intervessel pit
653 membrane in the stem of *Sapium sebiferum* (Euphorbiaceae). *IAWA Journal* **26**: 397–426.
- 654 **Plavcová L, Hacke UG.** **2012.** Phenotypic and developmental plasticity of xylem in hybrid
655 poplar saplings subjected to experimental drought, nitrogen fertilization, and shading. *Journal of*
656 *Experimental Botany* **63**: 6481–6491.
- 657 **Plavcová L, Jansen S, Klepsch M, Hacke UG.** **2013.** Nobody’s perfect: can irregularities in pit
658 structure influence vulnerability to cavitation? *Frontiers in Plant Science* **4**: 453.
- 659 **Roth-Nebelsick A.** **2019.** It’s contagious: calculation and analysis of xylem vulnerability to
660 embolism by a mechanistic approach based on epidemic modeling. *Trees*.
- 661 **Sanchez-Martinez P, Martínez-Vilalta J, Dexter KG, Segovia RA, Mencuccini M.** **2020.**
662 Adaptation and coordinated evolution of plant hydraulic traits. *Ecology Letters* **23**: 1599–1610.

- 663 **Sano Y. 2005.** Inter- and intraspecific structural variations among intervacular pit membranes,
664 as revealed by field-emission scanning electron microscopy. *American Journal of Botany* **92**:
665 1077–1084.
- 666 **Satarifard V, Grafmüller A, Lipowsky R. 2018.** Nanodroplets at membranes create tight-
667 lipped membrane necks via negative line tension. *ACS Nano* **12**: 12424–12435.
- 668 **Schenk HJ, Espino S, Romo DM, Nima N, Do AYT, Michaud JM, Papahadjopoulos-
669 Sternberg B, Yang J, Zuo YY, Steppe K, et al. 2017.** Xylem surfactants introduce a new
670 element to the cohesion-tension theory. *Plant Physiology* **173**: 1177–1196.
- 671 **Schenk HJ, Michaud JM, Mocko K, Espino S, Melendres T, Roth MR, Welti R, Kaack L,
672 Jansen S. 2021.** Lipids in xylem sap of woody plants across the angiosperm phylogeny. *The
673 Plant Journal* doi: 10.1111/tpj.15125.
- 674 **Schenk HJ, Steppe K, Jansen S. 2015.** Nanobubbles: a new paradigm for air-seeding in xylem.
675 *Trends in Plant Science* **20**: 199–205.
- 676 **Schmid R, Machado RD. 1968.** Pit membranes in hardwoods—Fine structure and development.
677 *Protoplasma* **66**: 185–204.
- 678 **Scholz A, Rabaey D, Stein A, Cochard H, Smets E, Jansen S. 2013.** The evolution and
679 function of vessel and pit characters with respect to cavitation resistance across 10 *Prunus*
680 species. *Tree Physiology* **33**: 684–694.
- 681 **Schuldt B, Buras A, Arend M, Vitasse Y, Beierkuhnlein C, Damm A, Gharun M, Grams
682 TEE, Hauck M, Hajek P, et al. 2020.** A first assessment of the impact of the extreme 2018
683 summer drought on Central European forests. *Basic and Applied Ecology* **45**: 86–103.
- 684 **Schuldt B, Knutzen F, Delzon S, Jansen S, Müller-Haubold H, Burlett R, Clough Y,
685 Leuschner C. 2016.** How adaptable is the hydraulic system of European beech in the face of
686 climate change-related precipitation reduction? *New Phytologist* **210**: 443–458.
- 687 **Shane MW, McCully ME, Canny MJ. 2000.** Architecture of branch-root junctions in maize:
688 structure of the connecting xylem and the porosity of pit membranes. *Annals of Botany* **85**: 613–
689 624.
- 690 **Sorek Y, Greenstein S, Netzer Y, Shtein I, Jansen S, Hochberg U. 2021.** An increase in
691 xylem embolism resistance of grapevine leaves during the growing season is coordinated with
692 stomatal regulation, turgor loss point and intervessel pit membranes. *New Phytologist* **229**: 1955–
693 1969.
- 694 **Sperry JS, Hacke UG. 2004.** Analysis of circular bordered pit function I. Angiosperm vessels
695 with homogenous pit membranes. *American Journal of Botany* **91**: 369–385.
- 696 **Sperry JS, Hacke UG, Pittermann J. 2006.** Size and function in conifer tracheids and
697 angiosperm vessels. *American Journal of Botany* **93**: 1490–1500.

- 698 **Sugiyama Y, Nagashima Y, Wakazaki M, Sato M, Toyooka K, Fukuda H, Oda Y. 2019.** A
699 Rho-actin signaling pathway shapes cell wall boundaries in Arabidopsis xylem vessels. *Nature*
700 *Communications* **10**: 468.
- 701 **Sugiyama Y, Wakazaki M, Toyooka K, Fukuda H, Oda Y. 2017.** A novel plasma membrane-
702 anchored protein regulates xylem cell-wall deposition through microtubule-dependent lateral
703 inhibition of Rho GTPase domains. *Current Biology* **27**: 2522-2528.e4.
- 704 **Thonglim A, Delzon S, Larter M, Karami O, Rahimi A, Offringa R, Keurentjes JJB,**
705 **Balazadeh S, Smets E, Lens F. 2020.** Intervessel pit membrane thickness best explains variation
706 in embolism resistance amongst stems of Arabidopsis thaliana accessions. *Annals of Botany*.
- 707 **Tixier A, Herbette S, Jansen S, Capron M, Tordjeman P, Cochard H, Badel E. 2014.**
708 Modelling the mechanical behaviour of pit membranes in bordered pits with respect to cavitation
709 resistance in angiosperms. *Annals of Botany* **114**: 325–334.
- 710 **Torres-Ruiz JM, Cochard H, Choat B, Jansen S, López R, Tomášková I, Padilla-Díaz CM,**
711 **Badel E, Burlett R, King A, et al. 2017.** Xylem resistance to embolism: presenting a simple
712 diagnostic test for the open vessel artefact. *New Phytologist* **215**: 489–499.
- 713 **Trueba S, Delzon S, Isnard S, Lens F. 2019.** Similar hydraulic efficiency and safety across
714 vesselless angiosperms and vessel-bearing species with scalariform perforation plates. *Journal of*
715 *Experimental Botany* **70**: 3227–3240.
- 716 **Vilagrosa A, Cortina J, Gil-Pelegrín E, Bellot J. 2003.** Suitability of drought-preconditioning
717 techniques in mediterranean climate. *Restoration Ecology* **11**: 208–216.
- 718 **Wason JW, Anstreicher KS, Stephansky N, Huggett BA, Brodersen CR. 2018.** Hydraulic
719 safety margins and air-seeding thresholds in roots, trunks, branches and petioles of four northern
720 hardwood trees. *New Phytologist* **219**: 77–88.
- 721 **Wheeler JK, Huggett BA, Tofte AN, Rockwell FE, Holbrook NM. 2013.** Cutting xylem under
722 tension or supersaturated with gas can generate PLC and the appearance of rapid recovery from
723 embolism. *Plant, Cell & Environment* **36**: 1938–1949.
- 724 **Wheeler JK, Sperry JS, Hacke UG, Hoang N. 2005.** Inter-vessel pitting and cavitation in
725 woody Rosaceae and other vesselless plants: a basis for a safety versus efficiency trade-off in
726 xylem transport. *Plant, Cell & Environment* **28**: 800–812.
- 727 **Yang J, M Michaud J, Jansen S, Schenk HJ, Zuo YY. 2020.** Dynamic surface tension of
728 xylem sap lipids. *Tree Physiology* **40**: 433–444.
- 729 **Zhang Y, Carmesin C, Kaack L, Klepsch MM, Kotowska M, Matei T, Schenk HJ, Weber**
730 **M, Walther P, Schmidt V, et al. 2020.** High porosity with tiny pore constrictions and
731 unbending pathways characterize the 3D structure of intervessel pit membranes in angiosperm
732 xylem. *Plant, Cell & Environment* **43**: 116–130.

- 733 **Zhang Y, Klepsch M, Jansen S. 2017.** Bordered pits in xylem of vesselless angiosperms and
734 their possible misinterpretation as perforation plates. *Plant, Cell & Environment* **40**: 2133–2146.
- 735 **Zhang H, Zhao C, Li Z, Li J. 2016.** The fiber charge measurement depending on the poly-
736 DADMAC accessibility to cellulose fibers. *Cellulose* **23**: 163–173.
- 737 **Zimmermann MH. 1983.** *Xylem Structure and the Ascent of Sap*. New York: Springer-Verlag.
- 738

739 **Table 1.** Overview of pit membrane thickness values (T_{PM} , nm) and their corresponding numbers
 740 of microfibril layers (N_L) according to the shrinkage model of Zhang et al. (2020). Assuming a
 741 homogeneous distribution of cellulose fibres, which have a diameter of 20 nm and a distance of
 742 20 nm from each other, $N_L = (T_{PM} + 20) / 40$.

T_{PM} [nm]	140	300	460	620	780	940	1100	1260
N_L	4	8	12	16	20	24	28	32

743

744

745 **Table 2:** Overview of the abbreviations of modelling and experimental parameters used with
 746 reference to their units and definitions.

Modelling acronyms	Units	Definition
Eqn		Equation
n		Sample size
N_C	/	Number of constrictions in a pore, which equals N_L
N_{HOLES}	/	Number of large, non-overlapping holes with random positions in a single pit membrane layer
N_L	/	Number of microfibril layers in a pit membrane; $N_L = (T_{\text{PM}} + 20) / 40$
N_P	/	Total number of pores in an intervessel pit membrane
N_{PIT}	/	Average number of intervessel pits for a vessel with average length and diameter
P	/	Probability of encountering at least one hole larger than a given threshold in any given layer of a pit membrane.
P_{LP}	/	Probability of a leaky pit membrane occurring in an average vessel
R_{MIN}	nm	Radius of the narrowest constriction in a pore
$R_{\text{MIN_max}}$	nm	Maximum R_{MIN} value of all pores in a single pit membrane
$R_{\text{MIN_mean}}$	nm	Mean R_{MIN} value of all pores in a single pit membrane
t	/	Minimal size of a pore, a pore constriction, or a hole to be considered as ‘large’
μ_R, σ_R, R_L	nm	Parameters of the left-truncated normal distribution modelling pore constriction radii in Model 1
Experimental acronyms	Units	Definition

A_P	mm ²	Total intervessel pit membrane surface area for a vessel with average length and diameter
D_P	μm	Diameter of an average intervessel pit membrane
P_{12}, P_{50}, P_{88}	MPa	Xylem water potential corresponding to 12%, 50% and 88% loss of maximum hydraulic conductivity, respectively
S	%/MPa	Slope of a vulnerability curve
$T_{PM_mean},$ $T_{PM_centre},$ T_{PM_edge}	nm	Intervessel pit membrane thickness as measured on TEM images of freshly embedded xylem samples; mean value, value around the centre, and near the edges of a pit membrane (excluding pit membrane annuli)
σ_R		Standard deviation

748 **Table 3.** Overview of the r - and R^2 -values between pit anatomical characteristics and embolism
 749 resistance. Anatomical measurements include mean values of the intervessel pit membrane
 750 thickness (T_{PM_mean}), central pit membrane thickness (T_{PM_centre}), and pit membrane thickness
 751 near the annulus (T_{PM_edge}). Embolism resistance is quantified as the xylem water potential
 752 values corresponding to 12% (P_{12}), 50% (P_{50}), and 88% (P_{88}) loss of the maximum hydraulic
 753 conductivity based on vulnerability curves. The estimation of embolism propagation pressure
 754 (EP) is either based on the largest value of R_{MIN} across all pores of a membrane (EP R_{MIN_max}) or
 755 the mean value of R_{MIN} across all pores of a membrane (EP R_{MIN_mean}), using a modified Young-
 756 Laplace equation. Only the regressions and correlations that show the strongest relation are given
 757 here. Logarithmic regression¹; power regression²; Pearson Coefficient Correlation³; p-values: <
 758 0.05 = *, < 0.01 = **, < 0.001***. Acronyms follow Table 2.

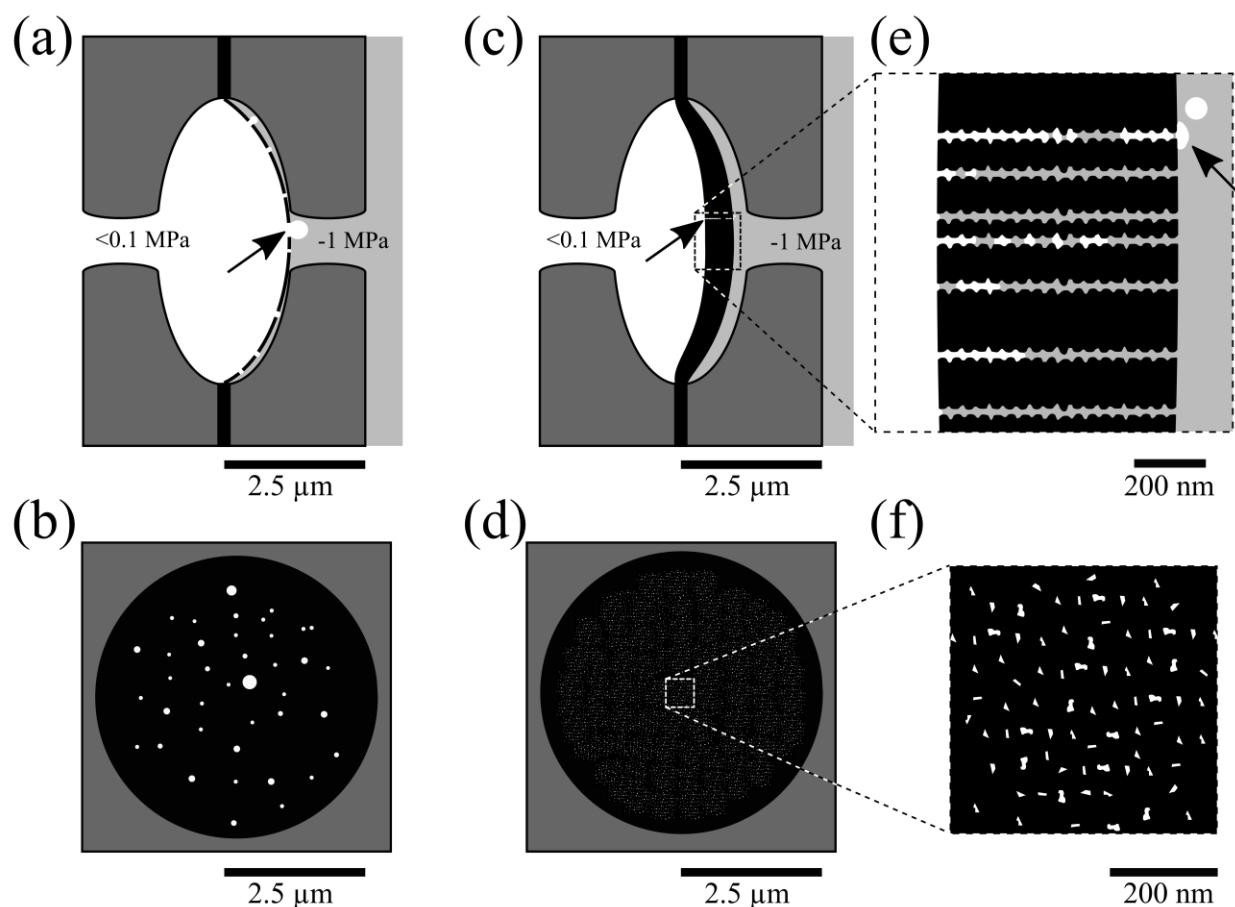
	P_{12}	P_{50}	P_{88}	S	T_{PM_centre} range
T_{PM_centre}	0.46 *** ¹	0.57 *** ¹	0.54 *** ¹	0.49 *** ²	0.79 *** ³
T_{PM_mean}	0.44 *** ¹	0.56 *** ¹	0.53 *** ¹	0.48 *** ²	n.a.
T_{PM_edge}	0.31 ** ¹	0.41 *** ¹	0.39 *** ¹	0.34 *** ²	n.a.
A_P	0.30 * ¹	0.25 * ¹	0.22 * ¹	0.10 *** ²	n.a.
EP R_{MIN_max}	0.64 *** ³	0.73 *** ³	n.a.	n.a.	n.a.
EP R_{MIN_mean}	0.67 *** ³	0.74 *** ³	n.a.	n.a.	n.a.

759

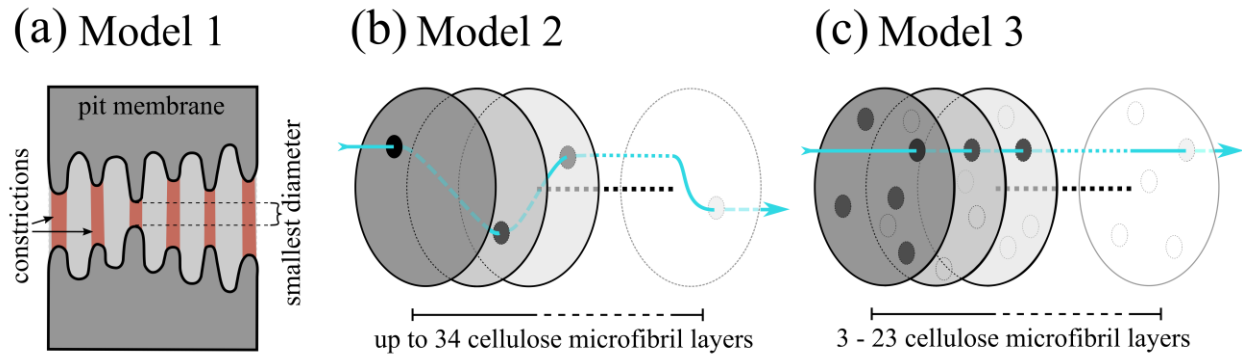
760 **Table 4.** Pearson correlation matrix presenting the r values of linear correlations between
 761 embolism resistance ($-P_{12}$, $-P_{50}$, $-P_{88}$), average intervessel pit membrane surface area per vessel
 762 (A_P), and pit membrane thickness measurements (T_{PM_mean} , T_{PM_centre} , T_{PM_edge}). Only 20 species
 763 for which we obtained A_P values were considered. For a correlation matrix based on an extended
 764 dataset ($n = 31$ species), see Table S1. Since T_{PM_mean} is calculated based on the thickness at the
 765 centre and the edge, correlations between T_{PM_mean} with T_{PM_centre} and T_{PM_edge} should not be
 766 considered and are given in brackets. Acronyms follow Table 2.

	A_P	T_{PM_mean}	T_{PM_centre}	T_{PM_edge}	$-P_{12}$	$-P_{50}$	$-P_{88}$
A_P	1						
T_{PM_mean}	-0.44	1					
T_{PM_centre}	-0.48*	(1.00**)	1				
T_{PM_edge}	-0.32	(0.96**)	0.94**	1			
$-P_{12}$	-0.33	0.72**	0.75**	0.58**	1		
$-P_{50}$	-0.40	0.83**	0.85**	0.70**	0.92**	1	
$-P_{88}$	-0.36	0.81**	0.83**	0.70**	0.90**	0.99**	1

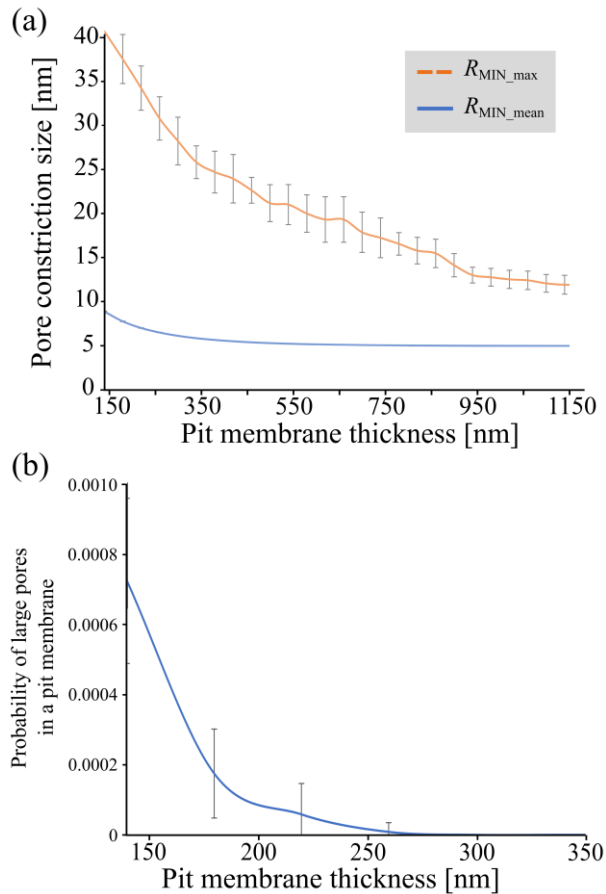
*, $p < 0.05$; **, $p < 0.01$

768 **Figures**

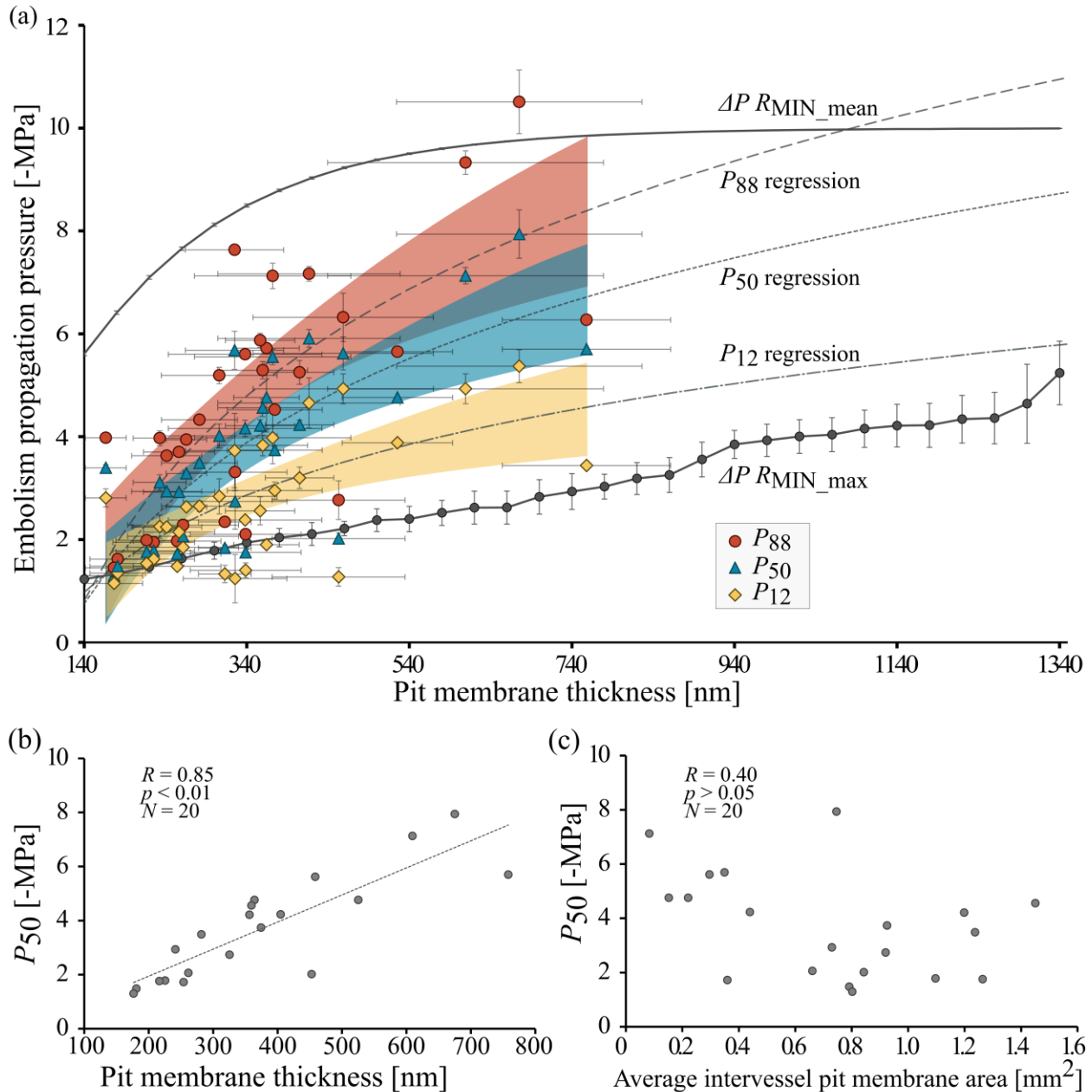
769 **Figure 1.** Drawings illustrating a mainly two-dimensional (a, b) and three-dimensional (c, d, e, f)
 770 concept of angiosperm pit membranes and embolism spreading under aspiration. The upper images
 771 (a, c, e) show a longitudinal view, while the bottom ones (b, d, f) represent frontal views. Large,
 772 cylindrical pores with circular cross-sections occur in a pit membrane, with no defined thickness,
 773 and the largest pore triggers air-seeding (arrows in a), or with a particular thickness and a three-
 774 dimensional concept of embolism propagation (c, e). Pores in a 670 nm thick pit membrane that is
 775 composed of multiple layers of cellulose fibrillar aggregates show multiple pore constrictions,
 776 which greatly reduces the size of the narrowest constriction within a pore (c, f). A magnified view
 777 is shown in e and f, with seven hypothetical pores illustrating some of the shortest hydraulic paths
 778 (e), and with 18 pore constrictions per pore pathway (f). White colour = gas; bright grey = xylem
 779 sap; black = solid phase of the primary cell wall, middle lamella or pit membrane, dark grey =
 780 secondary cell wall.



781 **Figure 2.** Three mathematical models to investigate the functional link between pit membrane
 782 thickness and effective diameters of pores. Model 1 (a) is based on a random number model to
 783 estimate the size of the narrowest constrictions of pores that traverse an entire pit membrane. This
 784 model is run ten times following Scenario 1 and Scenario 2, which has small or large pore
 785 constrictions for 12,000 or 1,100 pores per pit membrane, respectively, and with 4 to 34
 786 constrictions per pore in 140 to 1,350 nm thick pit membranes. Model 2 (b) examines the
 787 probability of large pores in 3,000 to 400,000 intervessel pit membranes within an entire vessel.
 788 Pit membranes include up to 34 microfibril layers, assuming either a 0.25 or 0.5 chance of
 789 encountering a large hole in a single layer. This model is independent of the actual size of what
 790 we consider a large pore, and does not incorporate alignment of pore constrictions. Model 3 (c)
 791 evaluates the probability of encountering pores with a large effective radius at the vessel level (i.e.
 792 for 30,000 intervessel pits), with pit membranes consisting of 3 to 23 microfibril layers, assuming
 793 5 or 10 holes of 200 nm per layer. Alignment of holes was included in Model 3 by simulating
 794 random locations of holes in each pit microfibril layer, and requiring minimal overlap between
 795 consecutive holes to create a pore. Different shades of grey represent various microfibril layers,
 796 and a hypothetical flow path is indicated by the blue lines in (b) and (c).

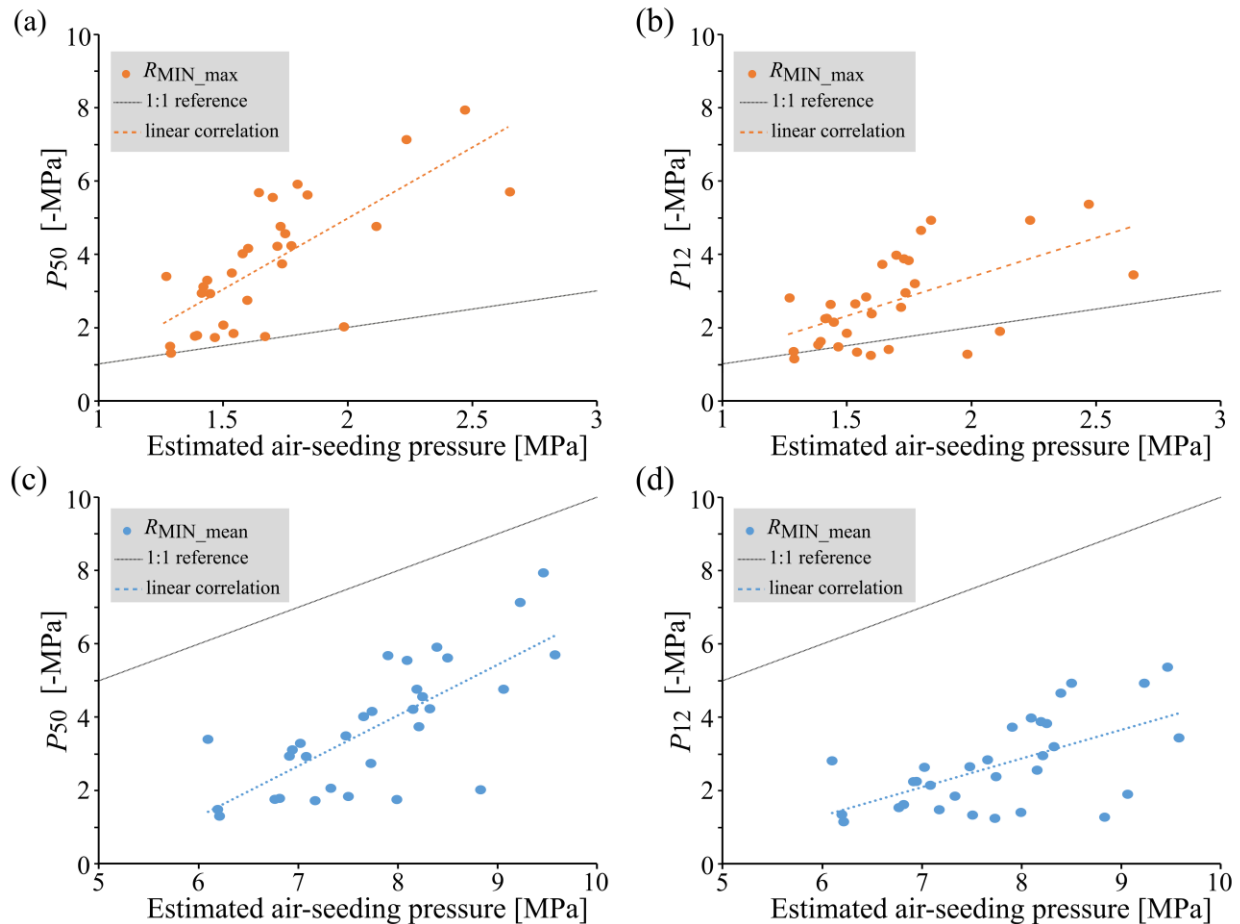


797 **Figure 3.** Results of Scenario 1 of Model 1, showing the pit membrane thickness plotted versus
 798 the pore constriction diameter based on Model 1 (a), and the likelihood of a relatively large
 799 R_{MIN_max} (≥ 17.5 nm) within a pit membrane (b), which decreased exponentially from $0.0008 \pm$
 800 0.0002 (SD) to values approaching zero with increasing pit membrane thickness. A random
 801 number model was used, with the mean pore constriction size set to 20 ± 15 nm, and a minimum
 802 size of 5 nm. Pore constriction sizes were determined ten times for 12,000 simulated pores,
 803 corresponding to an average sized pit membrane.

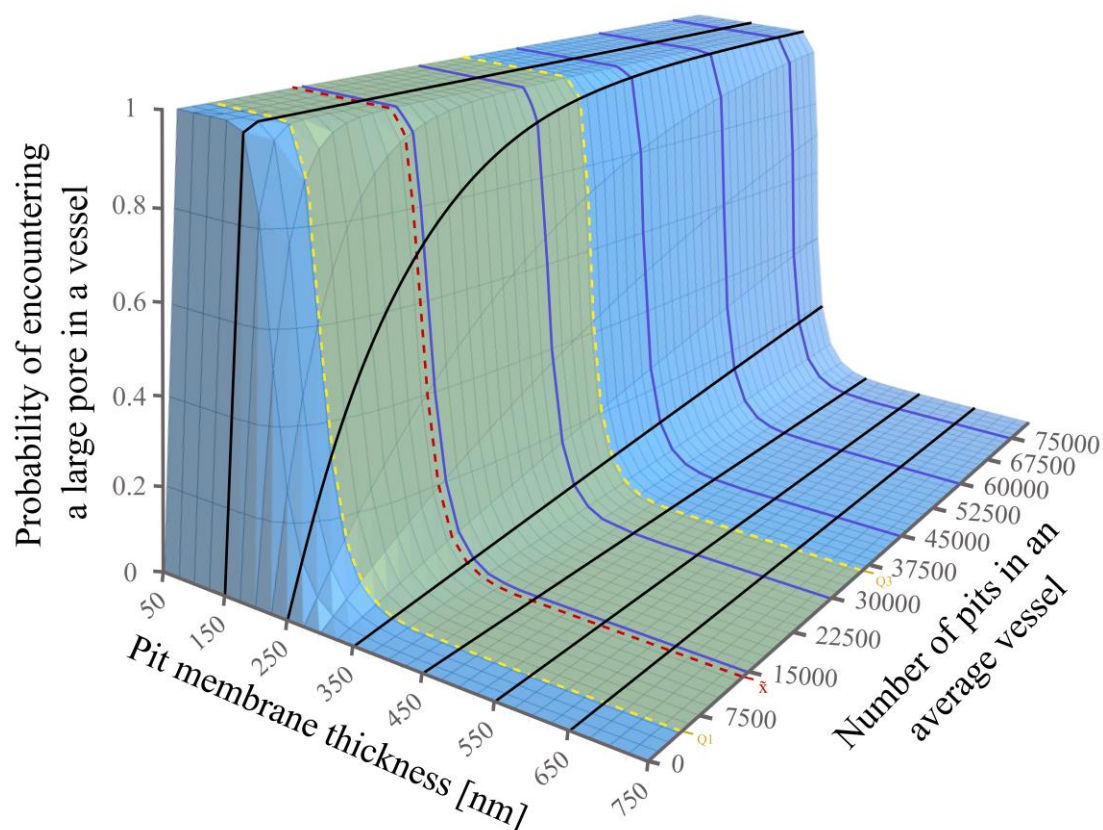


804 **Figure 4.** The relationship between central pit membrane thickness (T_{PM_centre}) with modelled and
 805 measured embolism resistance based on 31 angiosperm species (a) the relation of P_{50} -values and
 806 T_{PM_centre} (b) and P_{50} versus the intervessel pit membrane area per vessel (A_P , c). The species in
 807 graphs b and c are based on the same 20 species and can be directly compared. Modelled embolism
 808 propagation pressures rely on the largest value of R_{MIN_max} , and R_{MIN_min} with SD values (solid
 809 lines) based on all pores in a single pit membrane with variable thicknesses according to Model 1.
 810 A modified Young-Laplace equation is used to estimate the embolism propagation pressure for a
 811 surface tension of 25 mN/m (a). P_{12} , P_{50} and P_{88} values with SE values (intraspecific variability)

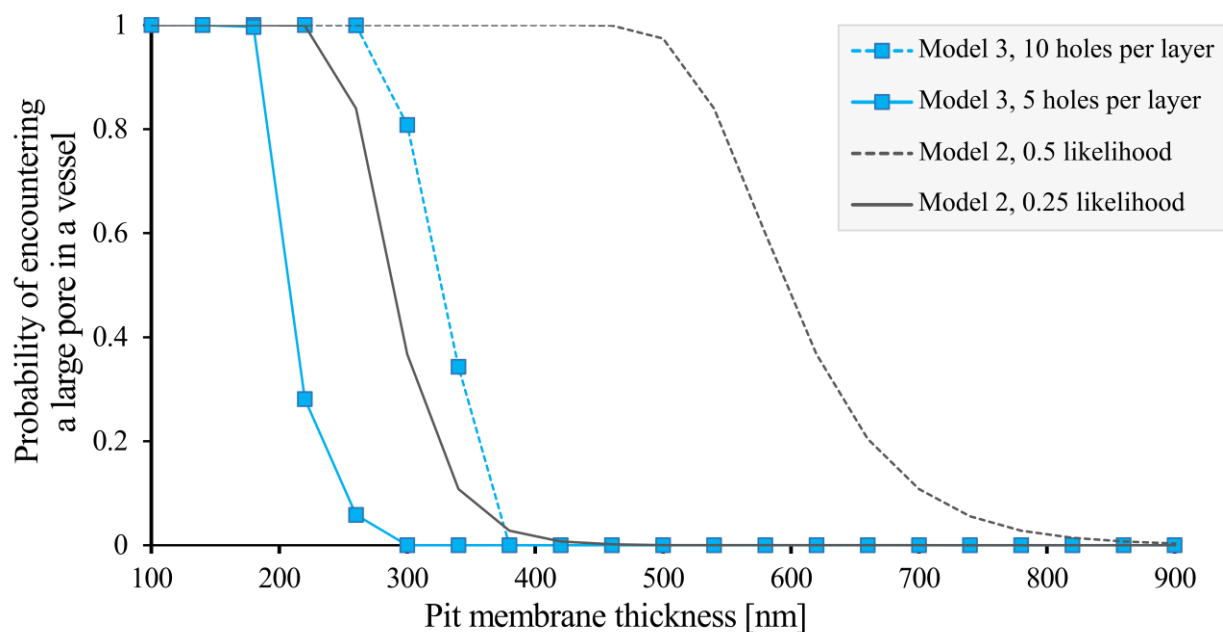
812 are based on a flow-centrifuge method or microCT images and plotted against T_{PM_centre}
 813 measurements with SD values (intra-tissue variability). T_{PM_centre} was based on TEM. Logarithmic
 814 regression lines are shown in grey, dashed lines, with corresponding confidence intervals ($P_{12} =$
 815 yellow, $P_{50} =$ blue, $P_{88} =$ red) in a. The values in b and c are given for a linear correlation.



816 **Figure 5.** Modelled embolism propagation pressure based on R_{MIN_max} (a, b; orange) and R_{MIN_mean}
 817 (c, d; blue) following Scenario 1 of Model 1 versus measured values of P_{50} (a, c; left) and P_{12} (b,
 818 d; right) for 31 angiosperm species. The 1:1 reference line is provided as a black, dotted line, and
 819 the linear regression line is blue, orange, and dashed.



820 **Figure 6.** The probability of encountering at least one pore with a large effective diameter in
 821 intervessel pit membranes for an entire vessel decreases with increasing pit membrane thickness
 822 (black lines), but increases with increasing number of pits (blue lines) according to Model 2. The
 823 likelihood of having a large hole within a single microfibril layer was assumed to be ≤ 0.25 . This
 824 model assumed that the number of cellulose layers in pit membranes increases with pit membrane
 825 thickness, did not consider the actual size of the pore constriction, and ignored whether or not a
 826 hole was aligned with other holes in adjacent pit membrane layers. The green area indicates where
 827 most angiosperm species occur based on the number of intervessel pits per vessel, with the median
 828 (red dotted line), and the first and third quartile (yellow dotted lines).



829 **Figure 7.** Comparison of the results from Models 2 and 3, showing for a wide range of pit
 830 membrane thicknesses the probability of encountering a large pore in a vessel with 30,000
 831 intervessel pits. For each model, 2 scenarios are given: A 0.25 and 0.5 likelihood of having a large
 832 hole in a pit membrane layer, without alignment of holes and no exact hole size (Model 2), and the
 833 occurrence of either five or 10 holes of 100 nm in diameter in a single pit membrane layer, with
 834 hole alignment as requirement (Model 3).

835

836

837 **Supporting Information**

838 Additional supporting information may be found in the online version of this article.

839 **Fig. S1** Frequency distribution of the number of intervessel pits for a vessel with average
840 dimensions and pit characteristics.

841 **Fig. S2** TEM images of intervessel pit membranes of different thickness.

842 **Fig. S3** Results of Model 1, Scenario 2; relation between T_{PM} and the size of a pore constriction.

843 **Fig. S4** Modelled embolism propagation pressure based on Model 1, with a surface tension of 72
844 mN/m.

845 **Fig. S5** Three-dimensional graph based on scenario 2 of Model 2, with a 0.5 probability of having
846 a large pore in a single pit membrane layer.

847 **Fig. S6** Two-dimensional graph based on Model 2 showing the probability of a large pore in a
848 vessel of up to 400,000 pits per vessel.

849 **Table S1** Dataset of the 31 angiosperm species studied, with reference to the anatomical and
850 hydraulic traits measured.

851 **Methods S1** Detailed model descriptions

852 **Methods S2** Model 1, excel function

853 **Methods S3** R script of Model 3

854 **Methods S4** Protocols: plant material, xylem embolism resistance, transmission electron
855 microscopy, vessel and pit characteristics

856 **Methods S5** Equation 3 and 4